Volume 5
Number 3
7 February 2024
Pages 833–1350

Materials Advances

rsc.li/materials-advances

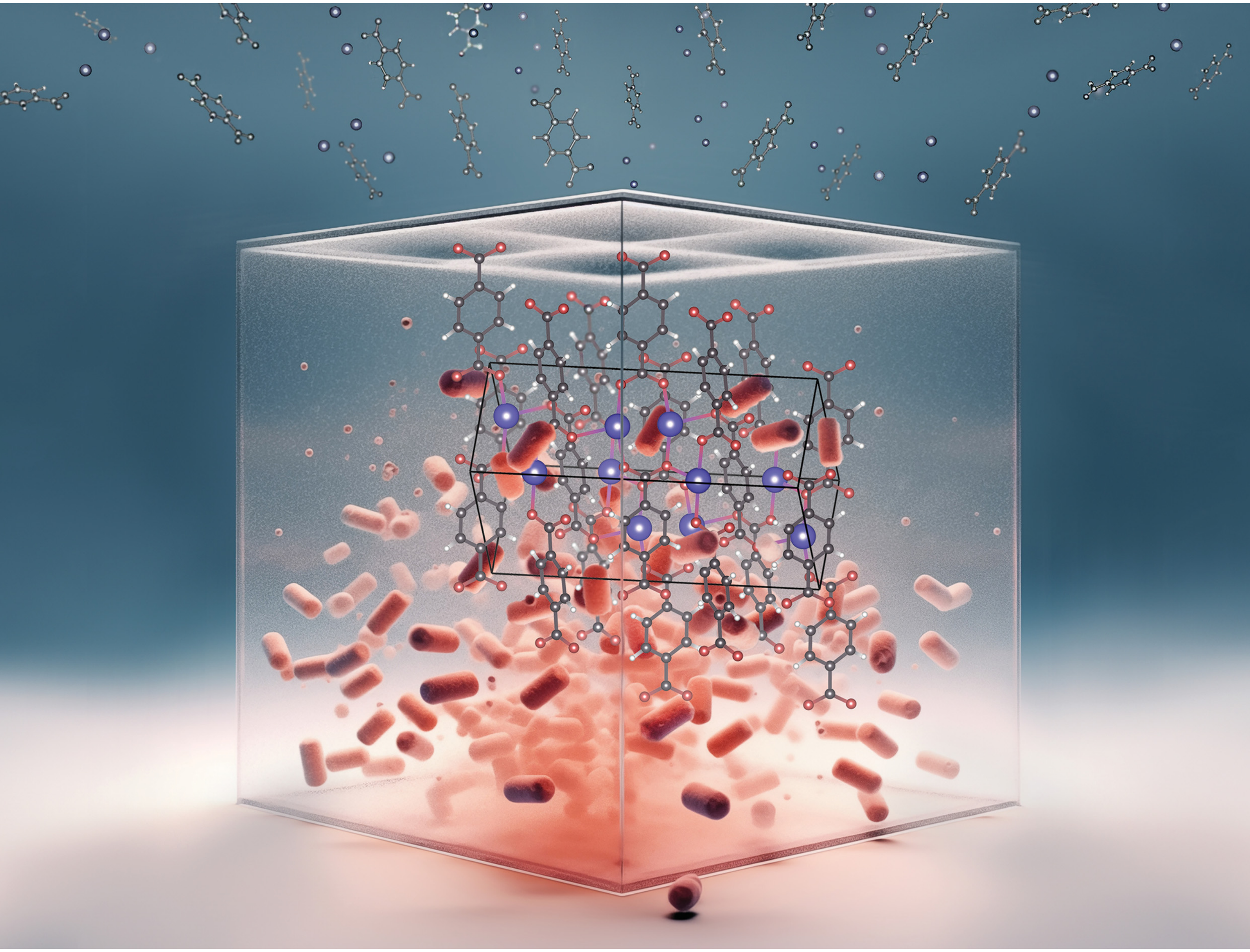

ISSN 2633-5409

ROYAL SOCIETY OF CHEMISTRY

PAPER
Guglielmo Guido Condorelli *et al.*
New metastable interfacial synthesis of a silver-terephthalate metal organic framework: structure, morphology and antibacterial activities

Materials Advances

ROYAL SOCIETY OF CHEMISTRY

PAPER

View Article Online
View Journal | View Issue

Cite this: *Mater. Adv.*, 2024, **5**, 1033

New metastable interfacial synthesis of a silver-terephthalate metal organic framework: structure, morphology and antibacterial activities†

Vincenzo Paratore, †[a] Domenico Franco,‡[b] Salvatore Guglielmino,[c]
Francesca Lo Presti,[a] Francesco Traina,[d] Sabrina Conoci [bef] and
Guglielmo Guido Condorelli *[ag]

In this work, a silver terephthalate-based metal organic framework, $[Ag_2(BDC)]_n$ (where H_2BDC is the terephthalic acid), has been obtained by new synthetic routes using terephthalic acid and silver salts dissolved in a dimethyl sulfoxide (DMSO)/water mixture in the presence of ammonia used to stabilize silver ions and to control their availability. Fast crystal growth was obtained at the metastable interface between the DMSO/water mixture and a water layer formed upon slow water addition. Chemical and morphological properties of the obtained MOFs depend on the adopted synthesis conditions (routes a–c), but in all cases $[Ag_2(BDC)]_n$ formation and growth took place by the dissolution of an ammonia hydrogen terephthalate salt. Large crystals of the ($[Ag_2(BDC)]_n$) monocline phase (named a-AgMOF) were grown through a slow (10 h) crystallization process (route a), while fast (3 h) crystallization processes (route b) lead to small size crystals with two different morphologies, named b-AgMOF. In order to obtain single crystal phases with a squared morphology, the Ag^+ availability was limited using potassium chloride (c(KCl)-AgMOF) and benzoic acid (c(BA)-AgMOF) as additives during the synthesis (route c). The chemical properties of the nanostructures were evaluated by transmission FTIR measurements, X-ray photoelectron spectroscopy (XPS), X-ray diffraction (XRD) and field emission scanning electron microscopy (FE-SEM). The obtained results indicate that all the obtained crystals possess efficient antibacterial activity. In particular, the b-AgMOF exhibited the highest efficiency against Gram-negative (*Pseudomonas aeruginosa* and *Escherichia coli*) and Gram-positive (*Staphylococcus aureus*) bacteria. In addition, the b-AgMOF showed good stability both in water (evaluated up to 84 days) and in different culture media (evaluated up to 24 hours), suggesting it as a promising candidate for use as a new antibacterial agent for several applications.

Received 7th August 2023,
Accepted 9th October 2023

DOI: 10.1039/d3ma00512g

rsc.li/materials-advances

Introduction

Research in the field of new antibacterial materials is the focus of ever-growing interest due to the capability of many bacteria to develop multidrug resistance (MDR). Nowadays, about 5 million deaths are associated with bacterial antimicrobial resistance (AMR) and this trend has been estimated to reach 10 million by 2050.[1] Several pathogenic bacteria, belonging to Gram-positive and Gram-negative, are able to "escape" common antibiotic therapies due to their increasing MDR.[2] Consequently, the associated infections are the major life-threatening cause, mainly for immunocompromised and critically ill patients.[3] In this regard, the acronym ESKAPE has been coined to include six highly virulent and antibiotic-resistant bacterial pathogens, namely *Enterococcus faecium*, *Staphylococcus aureus*, *Klebsiella pneumoniae*, *Acinetobacter baumannii*, *Pseudomonas aeruginosa*, and *Enterobacter spp.*[2] Among them, *P. aeruginosa* and *S. aureus* are some of the most ubiquitous pathogens in biofilms found in healthcare.[4]

---

[a] *Department of Chemical Science, University of Catania, v.le A. Doria 6, 95125, Catania, Italy. E-mail: guido.condorelli@unict.it*
[b] *Department of Chemical, Biological, Pharmaceutical and Environmental Sciences (ChiBioFarAm), University of Messina, Viale F. Stagno d'Alcontres 31, 98166 Messina, Italy*
[c] *IBMTech s.r.l., Via Alderaban 11A-95127, Catania, Italy*
[d] *Dipartimento di Scienze Biomediche e Neuromotorie-Alma Mater Studiorum—University of Bologna, Bologna, Italy*
[e] *Department of Chemistry "Giacomo Ciamician", Alma Mater Studiorum—University of Bologna, Bologna, Italy*
[f] *LAB Sense Beyond Nano—URT Department of Sciences Physics and Technologies of Matter (DSFTM) CNR, Messina, Italy*
[g] *Consorzio Interuniversitario di Scienze e Tecnologie dei Materiali (INSTM) UdR of Catania, Catania, Italy*

† Electronic supplementary information (ESI) available: XRD patterns, SEM images, and FTIR and deconvoluted XPS spectra. See DOI: **https://doi.org/10.1039/d3ma00512g**

‡ These authors contributed equally to this work.

Over the last few years, several strategies to overcome antimicrobial resistance have been developed, in order to obtain new broad-spectrum drugs with a better half-life.[5,6] *In vitro* studies have in fact demonstrated that nanomaterials exhibit toxic effects against several bacterial strains, thus indicating their potential as non-traditional biocidal agents in various biomedical applications.[7–10] Transition metal-based materials have been often chosen as antibacterial agents because of the combination of their excellent activity, stability, and human body tolerance.[11–14] Their antibacterial effects result from the metal ion release, which leads to cell membrane denaturation due to ROS generation or DNA intercalation.[15–17] Among these materials, silver nanoparticles have been widely used for their simple and versatile syntheses and high antibacterial yield.[18–21]

However, one of their drawbacks is the uncontrolled Ag^+ release in the environment, leading to metal accumulation and, therefore, to excessive cytotoxicity.[16,19] Some approaches are commonly followed to control silver ion release. One of them consists in the encapsulation of silver nanoparticles in organic coatings (such as carboxylic acids or thiol-based monolayers) which reduce the dissolution of free ions.[12,16,20,22] Another way is the use of coordination complexes in which the ions' release is controlled through the ligand–metal dissociation equilibrium.[22] Metal organic frameworks (MOFs) are particular compounds that can be considered coordination polymers with an ordered crystalline structure.[23–25] Compared with classical nanomaterials for antibacterial applications, MOFs show many advantages such as stable structures, on-demand degradation and efficient encapsulation of cargos, thanks to their porosity.[24,26] Specifically, only a few works have been reported on the synthesis of Ag-based MOFs (AgMOFs) for antibacterial applications which show a decreased cytotoxicity compared with Ag nanoparticles.[27–32] In these systems, the AgMOF can be considered as a metal ion reservoir which slows the release of Ag^+, thus generating a long-term antibacterial activity (Table 1).[28,33,34] One of the most used methods for the synthesis of MOFs is the solvothermal method which usually requires high temperature, a very long time and often toxic solvents.[15,35,36] Modulated synthesis techniques in which specific additives are added to the MOF precursor were also used to facilitate the crystallization process, but as for solvothermal methods, often a long-term reaction is required.[35–39]

In this article, we report new synthetics routes to prepare silver-based MOFs, $[Ag_2(BDC)]$ which use benzene-1,4-dicarboxylic acid (H_2BDC, also known as terephthalic acid) as an organic linker. As far as we know, only one paper reported the synthesis of these MOFs grown with a monoclinic structure ($P21/c$ space group) and no detailed information on their antibacterial activity was reported. The reaction reported by Sun *et al.* used a mixture of methanol and water at room temperature for one week to obtain an $Ag_2(BDC)$ MOF.[31] In our work, we developed a faster synthetic route compared with the previous one *via* crystallization at a metastable interface between water and a dimethyl sulfoxide (DMSO)/water solution and we also studied the correlations between synthesis parameters and crystal morphologies. Liquid–liquid synthesis at stable interfaces has been widely used for the preparation of various nanostructures,[40] whilst synthesis at metastable water–water interfaces is less common and few reports are available,[41] despite this approach possesses two important advantages: (i) easier purification compared to the separation from water immiscible organic solvents, which often contaminate the product surface; (ii) easy solubilization of salts.[40,41]

In our work, an $Ag_2(BDC)$ MOF (AgMOF) was obtained using as precursors terephthalic acid and silver nitrate dissolved in a dimethyl sulfoxide (DMSO)/water mixture in the presence of ammonia. Crystal growth occurred after a few hours at the metastable interface between the DMSO/water mixture and a film of water formed upon slow addition of water. The DMSO/water solution was chosen because of its lower toxicity compared to the methanol/water solution used in the previous paper. Two crystal morphologies were obtained as a function of synthetic conditions, and, in particular, with the conditions

Table 1 Antibacterial activity of the previously reported AgMOF and AgMOF-composites

Ref.	Silver-based MOF	Bacteria	MIC (μg mL^{-1})
27	$[Ag_2(Cedcp)]_n$	*E. coli* ATCC25922	>37.84
		P. aeruginosa ATCC27853	>37.84
		S. aureus ATCC 25923 (ATCC 6538)	37.84 (>37.84)
27	$\{[Ag_4(Cmdcp)_2(H_2O)_4]\cdot 4H_2O\}_n$	*E. coli* ATCC25922	
		P. aeruginosa ATCC27853	10.04
		S. aureus ATCC 25923 (ATCC 6538)	10.04
28	AgMOF(BTC)/GO nanocomposite	*E. coli* ATCC 35695	25
29	$[Ag_2(O\text{-}IPA)(H_2O)\cdot(H_3O)]_n$	*E. coli* F 1693	<10
		S. aureus F 1557	10
29	$[Ag_5(PYDC)_2(OH)]_n$	*E. coli* F 1693	10
		S. aureus F 1557	20
30	$[Cl@Ag_{14}(cPrC{\equiv}C)_{10}Cl_2\cdot(p\text{-}TOS)\cdot 1/3H_2O]_n$	*S. aureus*	10
33	AgMOF(BTC)	*E. coli* MG1655	16
33	AgMOF with N-CQDs composite	*E. coli* MG1655	4
33	AgMOF-N-CQDs hybrid	*E. coli* MG1655	8
33	AgMOF with S-CQDs composite	*E. coli* MG1655	8
33	AgMOF-S-CQDs hybrid	*E. coli* MG1655	16
	This work	*P. aeruginosa ATCC27853*	7.8–15.6
		E. coli ATCC 19138	7.8–15.6
		S. aureus ATCC 29213	31.3–62.6

adopted for the formation of a metastable interface between the water film and the DMSO/water solution. In addition, the AgMOF's antibacterial properties against *P. aeruginosa*, *E. coli* and *S. aureus*, quite common pathogens involved in a wide range of infections, including severe and often fatal hospital-acquired infections, were evaluated as a function of different synthesis methods used.

Materials and methods

Materials

$AgNO_3$ (Carlo Erba, Milan, Italy), terephthalic acid (H_2BDC, Sigma-Aldrich, Milan, Italy), dimethyl sulfoxide (DMSO, Sigma-Aldrich, Milan, Italy), a water solution of NH_3 (25 wt%, VWR Chemicals, Radnor, Pennsylvania, USA), benzoic acid (Sigma-Aldrich, Milan, Italy), KCl (Sigma-Aldrich, Milan, Italy) and HCl (33 wt%, Sigma-Aldrich, Milan, Italy) were all used without any purification.

Bacteria strain, media, and growth conditions: Pseudomonas aeruginosa ATCC27853 and *Escherichia coli* ATCC 19138 were purchased from the American Type Culture Collection (LGC Promochem, Milan, Italy) and cultured in Luria-Bertani broth (LB, Sigma-Aldrich, Milan). *Staphylococcus aureus* ATCC 29213 was purchased from the American Type Culture Collection (LGC Promochem, Milan, Italy) and cultured in tryptone soy broth (TSB, Sigma-Aldrich, Milan, Italy). Both strains were maintained in their respective media added with 20% glycerol at −80 °C. Thermogravimetric analyses were carried out using a Mettler Toledo TGA instrument with STARe software. All thermogravimetric experiments were repeated at least three times to confirm the accuracy and reproducibility of the data. About 6–7 mg of AgMOF was placed in an alumina crucible (40 μL). The samples were then heated at atmospheric pressure under purified nitrogen flow (50 sccm) with a 5 °C min^{-1} heating rate.

Synthesis of Ag_2(BDC) MOF

For all the synthesis routes of Ag_2(BDC), 77 mg of $AgNO_3$ was dissolved in 2 mL of NH_3 water solution (25 wt%) in an amber flask, then 4 mL of DMSO was added to the solution and stirred. Then 170 mg of H_2BDC was dissolved in 16 mL of DMSO. The two solutions were heated at 50 °C and the ligand's solution was slowly added to the metal solution under stirring at 50 °C. White crystals were formed when almost half ligand's solution was added as an intermediate reaction product. Then, three routes of synthesis were used: route a, route b, and route c. All crystals obtained during the synthesis were collected, filtered, and washed two times with DMSO, once with water and once with ethanol. To obtain dry powders, the crystals were kept in a vacuum vessel at 25 °C for a few hours. The obtained products were stored at room temperature in the dark until their characterization.

Route a: slow crystallization

H_2O (Milli-Q grade) was slowly dropped on the mixed $AgNO_3$/H_2BDC solution containing the intermediate product to obtain a thick metastable layer of water on the DMSO/water solution. This layered solution was heated at 70 °C for 10 h and water was constantly dropped to keep the layer for all the reaction time. After a few hours, the white precipitate at the bottom dissolved, colorless crystals were formed at the interface between the water layer and the H_2O/DMSO solution and precipitated slowly to the bottom. After 10 h, white crystals were obtained.

Route b: fast synthesis

A mixed $AgNO_3$/H_2BDC solution was placed in a closed chamber with a second beaker containing 10 mL of H_2O and the chamber was heated at 75 °C for 3 h. In this process, water vapors were slowly adsorbed on the DMSO/water solution and a thin water layer on the surface was obtained. As above, the formation of white crystals occurred at the interface between water and the DMSO/water solution. Crystalline powders were collected after 3 and 5 h.

Route c: modulated fast synthesis

The same procedure as described in route b was followed but with the addition at 50 °C and under stirring of KCl or benzoic acid to the $AgNO_3$ solution before mixing it with H_2BDC. Different concentrations of the additive were used: 2 mM, 4 mM, and 6 mM for KCl and 4 mM, 8 mM, and 12 mM for benzoic acid. After 3 h, light grey powders were obtained for KCl addition and light brown powders were obtained for benzoic acid addition.

Characterization

Transmission FT-IR measurements of samples in KBr pellets were carried out using a JASCO FTIR 4600LE spectrometer (Easton, MD, USA) in the spectral range 560–4000 cm^{-1} (resolution 4 cm^{-1}). X-Ray photoelectron spectroscopy (XPS) was carried out using a PHI 5000 Versa Probe Instrument (Chanhassen, MN, USA) using a monochromatic Al Kα X-ray source excited with a micro-focused electron beam. All the analyses were performed with a photoelectron take-off angle of 45 (relative to the sample Surface). The XPS binding energy (BE) scale was calibrated on the C 1s peak of adventitious carbon at 285.0 eV. XRD measurements were performed using an XRD Smartlab Rigaku diffractometer (Tokyo, Japan) in grazing incidence mode (0.5) using a rotating anode of Cu K source radiation at 45 kV and 200 mA. The SEM images were obtained using a field emission scanning electron microscope (FESEM) ZEISS VP 55 (Oberkochen, Germany). The (Brunauer–Emmett–Teller) methodology was used to determine the surface area of the samples towards the N_2 adsorption–desorption measurement at −196 °C using a Micromeritics Tristar II Plus 3020 instrument. The samples were pre-treated by out-gassing at 100 °C overnight.

Antibacterial assay

For each strain, semi-exponential broth culture was prepared at a final concentration of approximately 10^5 bacteria per mL starting from 0.5 Mc Farland inoculum (equivalent to 1.5×10^8 bacteria per mL). So, the prepared bacterial cultures were dispensed in 15 mL sterile tubes and added with increasing aliquots of AgMOF ranging from 3.9 to 250 μg mL^{-1}. To favor a better dispersion of the compound, the stock solution (1 mg mL^{-1}) was sonicated for 5 min in an ultrasonic bath. Then, 200 μL of the bacterial dispersion with the AgMOF was dispensed in wells of a 96 well plate (3 replicates for each experimental condition) and incubated at 37 °C for 18 h.

Minimum inhibitory concentration (MIC) was the lowest concentration at which compounds able to prevent visible bacterial growth. Starting from MIC endpoints, the minimum bactericidal concentration (MBC) was determined by subculturing on Mueller Hinton Agar (MHA; MHB added with 20 g L^{-1} of bacteriological agar) plates and was defined as the lowest concentration at which a compound can reduce bacterial viability by over 99.9% with respect to the initial inoculum.

In vitro stability of the AgMOF antibacterial activity was also evaluated over time in distilled water and cultural medium, which was LB for *P. aeruginosa* and *E. coli* and TSB for *S. aureus*. For studying the stability of the antibacterial activity in distilled water, batches of AgMOF suspension (at a concentration of 1 mg mL^{-1}) were prepared and stored in the dark and at room temperature for 1, 4 and 12 weeks, before being evaluated by an antimicrobial test. After the storage period, ability of each suspension for maintaining its bactericidal activity against previously tested bacterial strains was evaluated. In the tests conducted in culture media, increasing aliquots of AgMOF ranging from 3.9 to 250 μg mL^{-1} were incubated for 24 h in a fresh medium at 37 °C. After the incubation period, a final concentration of approximately 10^5 bacteria per mL was inoculated in each condition and incubated for an additional 18 hours at 37 °C. Then the antibacterial evaluation was carried out as described above.

A live/dead BacLight bacterial viability kit was also used to evaluate the bactericidal activity of the AgMOF. Briefly, semi-exponential broth culture at a final concentration of 0.5 Mc Farland (equivalent to 1.5×10^8 bacteria per mL) was exposed at MBC concentrations of AgMOF and incubated at 37 °C for 3 h. After the incubation period, 6 μL of the dye premixed of SYTO 9 (green-fluorescence staining viable cells) and propidium iodide (red-fluorescence staining dead cells), at a 1 : 1 ratio, was incubated with 200 μL of culture for 15 min at 37 °C. After the incubation period, the samples were visualized using a Leica DMRE epifluorescence microscope with a Leica C Plan 63× objective, using a BP 515–560 nm excitation filter in combination with an LP 590 nm suppression filter.

Results and discussion

The adopted approach for AgMOF synthesis leverages the formation of an interface between water and a DMSO/water mixed solution to promote MOF crystallization. In this method, the MOF precursors, Ag^+ and the organic ligand (H_2BDC), are first dissolved in the DMSO/water solution. Then, upon adding water on top of the DMSO/water solution, the metal ions diffuse into the aqueous phase, while the organic ligand remains in the DMSO solution, creating an interface between Ag^+ and H_2BDC rich solutions. The role of the reaction interface on the structure and morphology of the obtained materials was studied by varying experimental conditions (routes a–c in Fig. 1) in terms of water content and presence of additives. In particular, the concentration of reactants at the interface, which is a key nucleation factor, depends on the volume of water added to the DMSO solution. In route ***a***, a thick layer of water is maintained constantly through continuous water droplet addition on the surface. On the other hand, in route ***b***, the concentration of ions is increased by using a very thin layer of water. This thin layer is achieved by the adsorption of water vapor (see the Materials and Methods section).

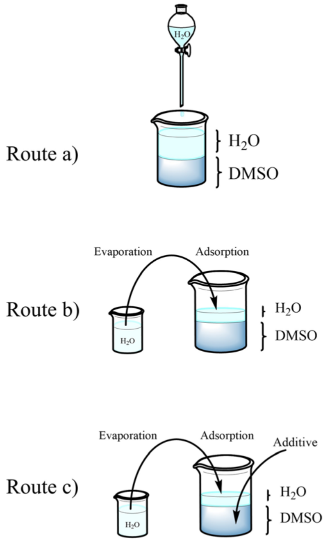

Fig. 1 Representation of the proposed AgMOF synthetic routes: (a) slow, (b) fast, and (c) modulated.

In the third synthesis, route c, the study focuses on modifying the outcome of route b by introducing additives into the solution.

Additives (namely KCl and benzoic acid) were used to limit the availability of Ag^+ ions and in turn to control the crystallinity of AgMOFs (route c). We will refer to these AgMOFs obtained through different routes as a-AgMOF for the product of route a; b-AgMOF, b5h-AgMOF for the products of route b obtained after 3 and 5 h, respectively; c(KCl)-AgMOF, c(BA)-AgMOF for the products of route c obtained with KCl and benzoic acid (BA) as additives, respectively.

In all routes, after adding the ligand's solution to the $AgNO_3$/NH_3 DMSO solution, white insoluble crystals are formed. These intermediate products dissolve during heating, leading to the formation of AgMOF crystals. To understand the growth process, the white intermediate obtained before adding water was separated and characterized. The XRD pattern (Fig. 2a) of the intermediate product is consistent with the presence of ammonium terephthalate monoacid salt.

The structure of NH_4HBDC, according to J.A. Kaduk *et al.*,[42] is reported in Fig. 2d. It consists of chains of $HBDC^-$ ligands kept together by a network of H-bonds with other ligands and NH_4^+ cations. The terephthalate ligands coordinate one NH_4^+ cation with one of their oxygens (monodentate coordination) and half of the carboxylic groups are randomly deprotonated.

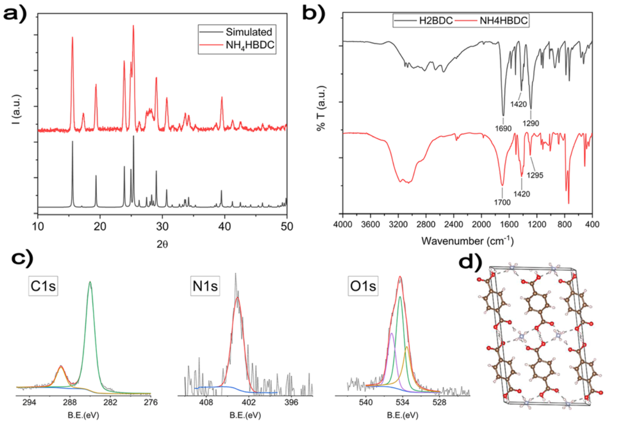

Fig. 2 (a) Comparative XRD patterns of reference NH_4HBDC (black) and white products identified as NH_4HBDC. (b) Comparative IR spectra of H_2BDC (black) and white products identified as NH_4HBDC (red). (c) XPS characterization of the intermediate product. (d) Crystal structure of the ammonium terephthalate salt.

Both XPS and FT-IR spectra performed to fully characterize the white precipitate are consistent with the reported NH_4HBDC structure. In FTIR spectra (Fig. 2b), the strong and broadened band in the 3400–2800 cm^{-1} range is consistent with the presence of HO^- and HN stretches involved in a network of H-bonds. The strong C=O stretch around 1700 cm^{-1} is similar but is slightly broader compared with the starting H_2BDC ligands, as expected for bi-carboxylic acids either not deprotonated or deprotonated with a monodentate coordination for which the C=O group is preserved.[43] C1s, N1s and O1s XPS spectral regions are reported in Fig. 2c. The C1s XPS spectrum shows two peaks. The first peak at 285 eV is due to the typical C–C/C–H hydrocarbon backbone and adventitious carbon. The second one at 289.3 eV is typical of carboxylic groups.[44–46] The BE value is higher than the one expected for deprotonated carboxylate groups,[45] due to only partial deprotonation and the H-bond network that usually increases the BE values. The N1s peak is observed at 401.6 eV consistent with ammonium ions.[45] The O 1s XPS band can be deconvoluted into three components: the first component at 531.4 eV can be attributed to the oxygen atoms of deprotonated OH groups, which have the highest electronic density. The second component at 532.5 eV corresponds to the presence of the carbonylic C=O groups and the third one at 533.9 eV is related to the oxygen in O–H groups.[47–49]

The formation of the $[(NH_4^+)(HBDC^-)]$ salt as an intermediate reaction product is due to the step shown in Scheme 1.

For all the reported routes, the intermediate carboxylate dissolves after a few hours and AgMOF was obtained according to Scheme 2.

$$AgNO_3 + NH_3 \xrightarrow{H_2O} Ag(NH_3)_2$$

$$H_2BDC + NH_3 \xrightarrow{DMSO/H_2O} [(NH_4)^+HBDC^-]\downarrow$$

Scheme 1 Schematic representation of the $[(NH_4^+)(HBDC^-)]$ formation.

$$[(NH_4)^+HBDC^-] + Ag(NH_3)_2 \xrightarrow{DMSO/H_2O;\,75°C} AgMOF$$

Scheme 2 Schematic representation of AgMOF synthesis by the $[(NH_4^+)(HBDC^-)]$ and $Ag(NH_3)_2$ reaction.

In route a, large AgMOF crystals (a-AgMOF) are formed after 10 hours. XRD, FT-IR, SEM and XPS characterization of the products is reported in Fig. 3.

XRD patterns (Fig. 3a) of a-AgMOF powders indicate the formation of crystalline Ag_2BDC with the monoclinic structure ($P21/c$ space group) according to the reported crystallographic data.[31] SEM analysis (Fig. 3d) shows the formation of well-shaped rhombohedral crystals with dimensions greater than 20 μm. The a-AgMOF FT-IR spectra (Fig. 3b) show two strong peaks at 1567 cm^{-1} and 1376 cm^{-1} which are shifted compared to the main peaks of the H_2BDC carboxylic group (C=O stretching at 1687 cm^{-1} and the C–OH stretching at 1288 cm^{-1}), thus suggesting the formation of carboxylate salt peaks.[50]

XPS spectra are consistent with the formation of the Ag terephthalate MOF. The C1s peak (Fig. 3c) shows the presence of three components: a component at 285.0 eV attributed to the C–C/C–H atoms and the adventitious carbon used as a BE scale reference, a component at about 286.0 is attributed to C–OH contaminants and the peak at 288.6 eV is related to carboxylate groups.[49,51] The O1s peak centred at 531.7 is attributed to the oxygen of the carboxylate groups. A shoulder at 533.0 eV can be also detected due to unreacted carboxylic acids and adsorbed water. The signals of the Ag3d 5/2 and 3/2 doublet peaks at 368.6 eV and 374.5 eV are related to the presence of Ag^+ ions.

Using route b, well-crystallized AgMOF particles were obtained after 5 hours (Fig. S1a, ESI†). In this case, the crystals (b5h-AgMOF) are smaller compared to those obtained using route a (Fig. S1b, ESI†), but they exhibit the same XRD pattern. By reducing the reaction time to 3 hours, the resulting MOF (b-AgMOF) displays all the XRD reflections observed in the a-AgMOF and b5h-AgMOF samples. However, two new peaks appear at 7.4° and 15° (Fig. 4a), indicating the formation of a

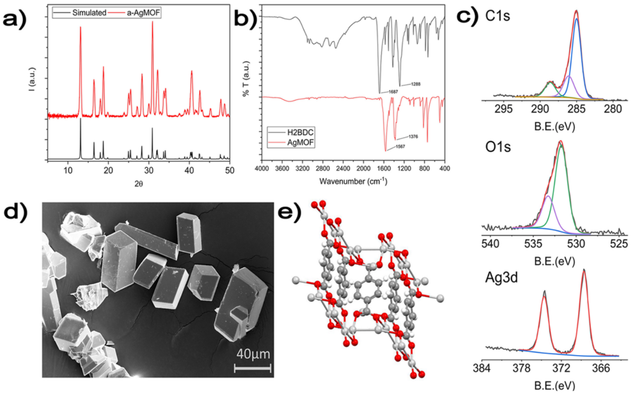

Fig. 3 (a) XRD analysis of the a-AgMOF and reference AgMOF pattern (CCDC identifier no. 198096);[31] (b) FT-IR spectra of a-AgMOF (red line) and H_2BDC (black line); (c) XPS analysis of a-AgMOF C1s, O1s and Ag3d peaks from right to left, respectively; (d) SEM pictures of a-AgMOF; (e) crystalline structure of the Ag_2BDC MOF.

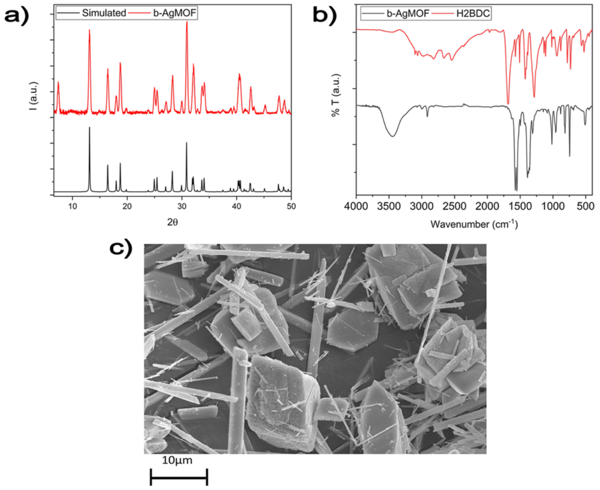

Fig. 4 (a) XRD pattern of b-AgMOF in red lines and reference curves in black lines; (b) comparison between the IR spectra of b-AgMOF (red) and ligand H_2BDC (black); (c) SEM pictures of the two crystalline phases obtained in b-AgMOF.

secondary phase. Furthermore, the SEM images (Fig. 4c) clearly indicate the presence of two types of crystal morphology. The first type exhibits big and square shapes similar to those observed in the a-AgMOF samples. The second type is smaller with a needle shape. The FT-IR images (Fig. 4b) show the typical carboxylate peaks at 1567 cm^{-1} and 1376 cm^{-1} and the XPS spectra show the carboxylates band at about 288.5 eV (Fig. S2, ESI†), thus confirming the deprotonation of the carboxylic groups and the formation of carboxylate salt.

Previous literature studies suggested that the addition of additives to the reaction mixture can improve the crystallization rate and control the crystal size, and for this reason synthesis route c was performed.[52–57]

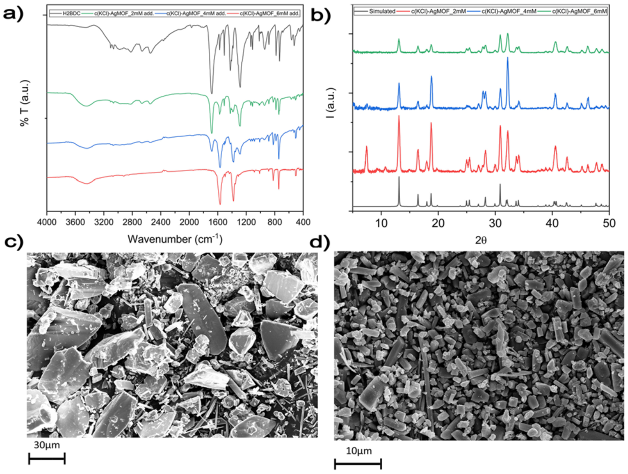

Fig. 5 (a) FT-IR spectra of c(KCl)-AgMOF at different KCl concentrations (the H_2BDC FT-IR spectrum was added as reference); (b) XRD analysis of c(KCl)-AgMOF at different concentrations of KCl; and SEM pictures of c(KCl)-AgMOF obtained using (c) 2 mM and (d) 6 mM KCl concentrations.

FT-IR spectra (Fig. 5a) show that the peak due to carboxylate groups increases upon increasing KCl concentration at the expense of carboxylic groups of the free H_2BDC, thus suggesting that KCl favours the formation of the coordination bond between the BDC ligands and silver ions.

In addition, the XRD patterns (Fig. 5b) show that by increasing KCl concentrations, the peaks of the pure Ag_2BDC monoclinic phase increase compared to the peaks at 7.4° and 15 due to the secondary phase. Specifically, the pure Ag_2BDC monocline phase was obtained in KCl (6 mM).

SEM analysis (Fig. 5c and d) confirms the XRD results. Two grain types were observed for low (2 mM) KCl concentrations, while using a higher KCl concentration (6 mM), only one crystal type was observed (Fig. 5d). Note that these crystals have smaller dimensions (less than 5 μm) than the ones obtained in route a and b and their dimension decrease as the modulator concentration increases.

Comparable results were obtained with benzoic acid (BA) as an additive (Fig. S3, ESI†). In fact, by increasing the benzoic acid concentration, the Ag_2BDC monocline phase formation was favoured compared to the secondary ones. However, in this case, we could not obtain a pure monocline phase because for BA concentrations higher than 8 mM, an extremely low amount of the product was obtained.

Both additives (BA and KCl) act as competitors of the terephthalate ligand in the silver ion complexations due to the presence of either carboxylic groups or the chloride ions. This behaviour favours the crystallization process of Ag_2BDC crystals by reducing the availability of the metal ions. These results show that it is possible to modulate the crystalline phases and morphologies of AgMOF by adjusting the amount of water, the reaction time, and the concentration of modulators such as BA and KCl. A notable difference between the two morphologies lies in their surface area. The BET analysis revealed that the b-AgMOF exhibited higher surface area compared to the single monocline phase Ag_2BDC of the a-AgMOF sample. The surface area values are 45.2 m^2 g^{-1} and 36.9 m^2 g^{-1} for b-AgMOF and a-AgMOF, respectively. In the TGA analysis presented in Fig. S6a and b (ESI†), a weight loss of approximately 3% is observed at around 100 °C for both b-AgMOF and c-AgMOF, indicating the desorption of water. Additionally, the TGA weight loss and the first derivative curves reveal that both MOFs undergo degradation, with c-AgMOF exhibiting a degradation of approximately 35% at 385 °C and b-AgMOF showing around 28% degradation at 400 °C. Notably, the most significant disparity between these two morphologies is observed in b-AgMOF, where there is an additional weight loss of 9.5% at around 220 °C. This weight loss step is attributed to the desorption of DMSO trapped within the porous structure of b-AgMOF, a phenomenon confirmed by EDX analysis presented in Table S1 (ESI†) in which the presence of solvent in the b-AgMOF is shown. These results suggest that the distinct morphologies of these MOFs may be linked to the presence of DMSO as a solvent, enabling the formation of different crystalline morphologies in a shorter synthesis time and without the use of additives.

Antibacterial evaluation

The antibacterial efficacy of the b-AgMOF was evaluated by biological assays against *P. aeruginosa*, *E. coli* and *S. aureus*, quite common pathogens involved in a wide range of infections, including severe and often fatal hospital-acquired infections. The results are summarized in Fig. 6.

Specifically, for Gram-negative bacteria, namely *P. aeruginosa* and *E. coli*, we found that the MIC value was 7.8 μg mL^{-1}. Although at 3.9 μg mL^{-1}, a visible and clear turbidity was observed for both bacterial strains, spectrometric evaluation at 540 nm (OD_{540}) indicated significant bactericidal activity, so that a viability reduction of 75% and 70% was observed for *P. aeruginosa* and *E. coli*, respectively. The MIC values were also confirmed by the MBC assay. Unlike Gram-negative strains, *S. aureus* showed greater resistance to AgMOF with a MIC value established at 31.3 μg mL^{-1}, while MBC at 62.5 μg mL^{-1}. Also, in this case, at a sub-MIC concentration of 15.6, we found a significant viability (approximately of 72%).

In order to understand the role of AgMOF formation in antibacterial activity, we have also evaluated the antibacterial activity of AgNO3 and the terephthalate ligand as terephthalic acid. We have estimated that 250 μg mL^{-1} of AgMOF should correspond to an equivalent of 223.7 μg mL^{-1} of AgNO3 and 109 μg mL^{-1} of the terephthalate ligand. No significant antibacterial activity was observed for terephthalic acid. For AgNO3, the antibacterial test indicated similar values for both Gram strains, namely 31.3 μg mL^{-1} for Gram-positive strains and 7.8 μg mL^{-1} for Gram-negative strains, when the metal salt was tested as soon as it was prepared. On the other hand, we observed a significant reduction in the bactericidal activity of the metal salt compared with AgMOF materials, especially against Gram-negative strains (62.5 μg mL^{-1} for the Gram-positive strain and 31.3 μg mL^{-1} for both Gram-negative strains) when evaluated over time in distilled water (after one week) and culture medium (after just 5 hours of incubation in fresh medium before bacterial inoculation).

It is known that metal–organic frameworks can act as a reservoir for metal ions which interact with the bacterial cell components.[58] Metal ions can diffuse inside the cell and interact with the cellular membrane/wall, cell macromolecules such as proteins and nucleic acids.[59] In addition, they can increase cytoplasmic levels of reactive oxygen species (ROS), such as hydrogen peroxide, superoxide anions and hydroxyl radicals, by altering the normal function of the respiratory chain in the cell.[60–66] Since the antibacterial effect is due to the release of silver ions from the metal organic framework structure, the different susceptibility of Gram-negative strains (*P. aeruginosa* and *E. coli*) compared to Gram-positive ones (*S. aureus*) is ascribable to different composition and organization of their cell wall. It has been reported that the different susceptibility of Gram-negative bacteria to silver nanoparticles (AgNPs) could be due to the presence of LPS molecules, which increase the negative charge of the cell membrane compared to Gram-positive bacteria.[67] Recent evidence has also suggested that the mosaic structure of LPS molecules in Gram-negative bacteria makes some regions more negatively charged so that NPs (positively charged) tend to aggregate in these areas, leading to a localized toxic effect.[68] On the other hand, the greater amount of peptidoglycan in Gram-positive bacteria provides greater resistance to damage from silver ions, due to their trapping by negatively charged peptidoglycan.[68] The latter should justify the different values found between MIC and MBC in *S. aureus*, showing that at MIC concentrations, there is only an inhibitory action, and a viable bacterial residue is retained. Consequently, when the biocidal agent is removed by subculturing in fresh medium, the bacterial strain resumes its rapid growth.

The results from the antibacterial assays agreed with those from live/dead staining (Fig. 7).

Also in this case, a noticeable difference emerged between Gram-negative (*P. aeruginosa* and *E. coli*) and Gram-positive (*S. aureus*) bacteria. In the case of *S. aureus*, the viability staining showed the presence of very few living bacteria (green fluorescent) and many dead (red fluorescent) bacteria in the presence of b-AgMOF after 3 hours (Fig. 7f). All bacteria in the presence of b-AgMOF were dead after an overnight (18 h) incubation (Fig. 7i). Otherwise, almost all cells were red fluorescent for *P. aeruginosa* (Fig. 7d) and *E. coli* (Fig. 7e) after just

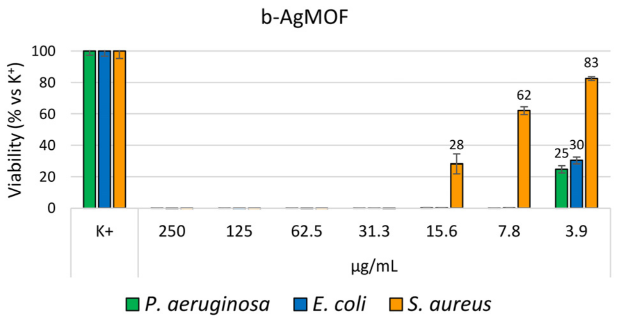

Fig. 6 Bacterial reduction of *P. aeruginosa*, *E. coli* and *S. aureus* exposed to b-AgMOF with concentrations ranging from 250 to 3.9 μg mL^{-1}.

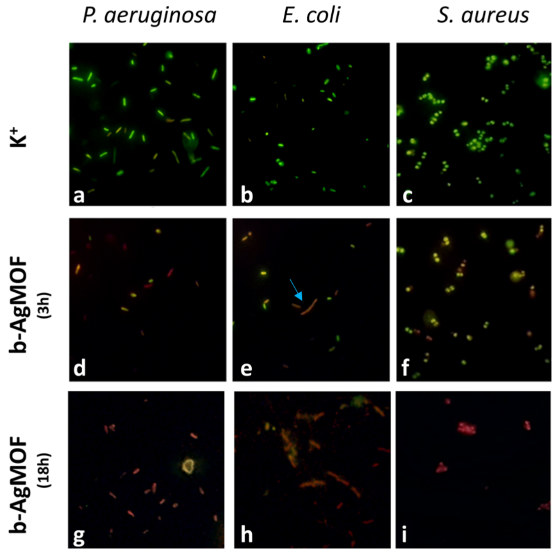

Fig. 7 Live/dead staining of *P. aeruginosa*, *E. coli* and *S. aureus* exposed to b-AgMOF at MIC values for 3 h and 18 h.

3 hours. Also in this case, all bacteria were dead after an overnight incubation with b-AgMOF (Fig. 7g and h). Intriguingly, we observed that bactericidal effects in *E. coli* could cause cellular filamentation (cyan arrow in Fig. 7e), while we did not observe any cell filamentation when *P. aeruginosa* was tested under the same conditions. These elongated cell shapes are more widespread after an overnight incubation. These findings, similarly, obtained by other authors with biocidal systems based on AgNPs, demonstrate a multivalent biocide effect towards *E. coli*, related to the inhibition of DNA synthesis and induction of SOS-mediated filamentation.[69,70]

Antimicrobial assays were also carried out with crystalline phase obtained by using KCl (6 mM, c(KCl)-AgMOF) and benzoic acid (8 mM, c(BA)-AgMOF) additives (Fig. 8).

Although antimicrobial assays indicated, also in this case, a strong antibacterial activity of the two AgMOFs against all bacterial strains, some considerations need to be made. First, both derived crystalline phases exhibit higher MIC values than b-AgMOF (Table 2).

An explanation could derive from the lower yield, in terms of Ag^+ ions' concentration, derived from the addition of the two additives. In our silver-based material systems, the antibacterial activity of AgMOF could be attributed to the leaching of ions from themselves which can diffuse inside the bacterial cells and interact with the cellular membrane/wall and other macromolecules such as proteins and nucleic acids.[71,72] In the case of c(BA)-AgMOF, the benzoic acid could act as a capping agent decreasing Ag^+ ion leaching and dissolution. On the other hand, the presence of Cl-residual ions (Fig. S4, ESI†) in c(KCl)-AgMOF could determine the formation of silver precipitates, which decreases the Ag^+ concentration. In both cases, the reduction of free Ag^+ ions could reduce bactericidal activity.

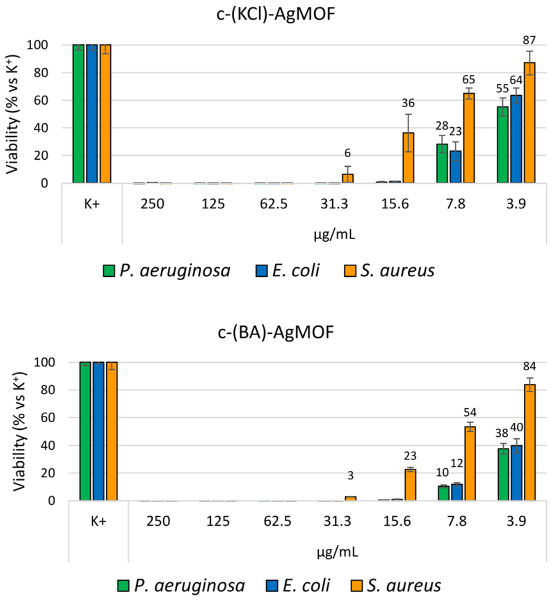

Fig. 8 Bacterial reduction of *P. aeruginosa*, *E. coli* and *S. aureus* exposed to c(KCl)-AgMOF and c(BA)-AgMOF with concentrations ranging from 250 to 3.9 µg mL^{-1}.

Table 2 Minimum inhibitory concentration (MIC) (µg mL^{-1}) of b-AgMOF, c(KCl)-AgMOF and c(BA)-AgMOF against *P. aeruginosa*, *E. coli* and *S. aureus*

Bacteria	b-AgMOF MIC	c(KCl)-AgMOF MIC	c(BA)-AgMOF MIC
P. aeruginosa	7.8	15.6	15.6
E. coli	7.8	15.6	15.6
S. aureus	31.3	62.6	62.6

Further analyses were performed to evaluate the stability of the antibacterial effect of the Ag-MOFs. In particular, the antibacterial effect of b-AgMOF, chosen for its lowest MIC and MBC values, was evaluated in distilled water for more than 80 days (Fig. 9).

Antimicrobial assays show, for all three bacteria tested, a loss of a dilution factor in the MIC only in the first week, while no significant reduction activity was observed after 84 days of aging of the same solution. In fact, MIC values were 15.6 µ mL^{-1} for *P. aeruginosa* and *E. coli* and 62.5 µ mL^{-1} for *S. aureus*. MIC values were also confirmed for MBC, indicating at such concentrations, an almost exclusively bactericidal effect. This finding is particularly interesting for *S. aureus*, whereby a difference between the MIC and MBC values was observed towards the freshly prepared suspensions. In this regard, further evaluations will serve to clarify the mechanisms underlying the biocidal effect of b-AgMOF towards *S. aureus*.

In any case, b-AgMOF appeared to have good stability in solution even for prolonged periods.

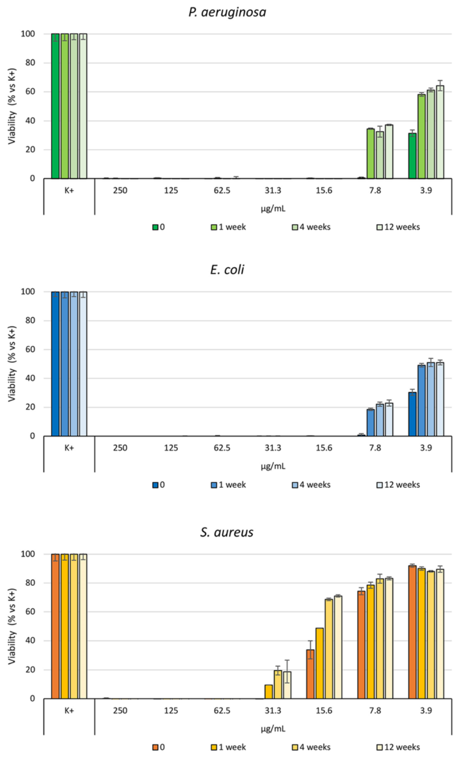

Fig. 9 Bacterial reduction of *P. aeruginosa*, *E. coli* and *S. aureus* exposed to b-AgMOF, with concentrations ranging from 250 to 3.9 µg mL^{-1}, stored for 0, 1, 4 and 12 weeks in the dark and at room temperature.

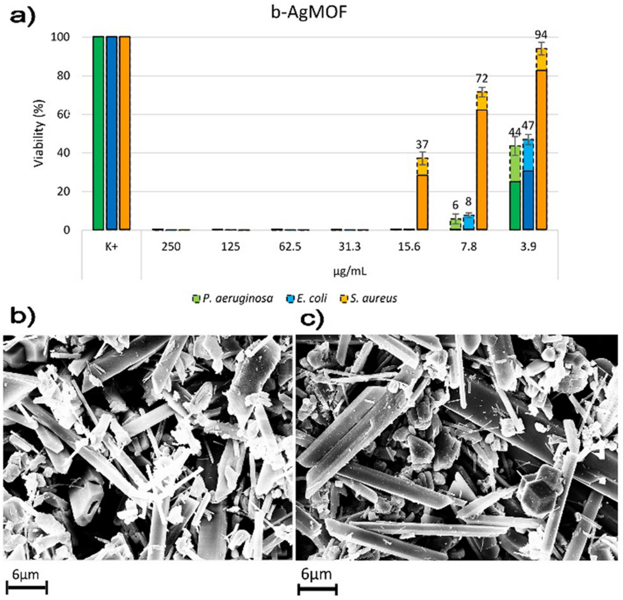

Fig. 10 (a) Bacterial reduction of *P. aeruginosa*, *E. coli* and *S. aureus* of b-AgMOF after *in vitro* stability for 24 h in the cultural medium before inoculation of bacterial strains. The continuous and dotted line histograms refer to b-AgMOF with concentrations ranging from 250 to 3.9 μg mL^{-1}, fresh and after an incubation period (24 h) in culture medium, respectively. (b) SEM picture of b-AgMOF and (c) b-AgMOF SEM picture after 24 h in the cultural medium.

One of the key issues related to colloidal solutions for antibacterial applications is their instability.[73,74] Stability depends on the capping agent and environmental conditions, such as pH and ionic strength.[75–77] In the case of AgNPs, several strategies have been investigated to improve the NP suspension stability, to prevent aggregation. In fact, it is known that sizes are critical to explicate antibacterial activity, due to large surface area/volume ratios (compared to larger NPs) that favour metal ions' release and ROS production.[10,78,79] On the other hand, smaller nanoparticles tend to aggregate more easily, reducing their bioavailability for biocidal activity. In addition, the release of ions from metal NPs is significantly influenced by the medium in which they are dispersed.[80] For example, it was found that chloride present in culture medium can favour ion release from AgNPs.[81] This behaviour leads to an initial increase in bactericidal activity, but it reduces the AgNPs' life and, consequently, limits the antibacterial action over time. Although AgMOFs are different systems compared with AgNPs, the colloidal stability is a critical parameter to evaluate their applicability as antibacterial agents. Thus, the atomic composition, morphologies, and antibacterial activity of AgMOFs were assessed following a 24 hours incubation period in the culture medium before the introduction of bacterial strains (Fig. 10).

The SEM image in Fig. 10 revealed no significant morphological alterations. However, through the use of EDX characterizations (Fig. S5 and Table S1, ESI†), it became evident that there was a gradual decrease in the carbonic component of the material, confirming its slow degradation in the cultural medium.

The antimicrobial assay shows a loss of a dilution factor in the MIC only for Gram-negative strains (*P. aeruginosa* and *E. coli*); while no significant reduction activity was observed for *S. aureus* compared to the results previously found for fresh suspensions. Similar results were obtained by different authors, although in most cases, a strong bactericidal activity is associated with a high release rate and a low service life of metal organic frameworks.[66] For example, Liu *et al.* introduced three Ag-based metal–organoboron frameworks with different topological structures, consisting of N-donor ligand tris-(4-pyridylduryl)-borane (L), Ag$^+$, and different coordination solvents.[82] They showed antimicrobial activities against *E. coli* and *S. aureus* with MIC values higher than 250 μg mL^{-1} and with a durability over 7 months in distilled water. An Ag-based metal organic framework reported by Lu *et al.*, consisting of 1*H*-benzimidazole with Ag–N coordination, showed bactericidal activity comparable to the present study, but with a durability of about a week.[83]

Conclusions

In this work, we find a new and less toxic synthetic method to obtain a silver-based MOF for antibacterial applications. New synthetic routes were developed to obtain fast crystallization in the 10–3 h range in a no toxic solvent (water/DMSO) mixture. Crystal growth occurred at the metastable interface between the DMSO/water mixture and a film of water formed upon the addition of water either drop by drop (route a) or from water vapours (routes b). The role of additives (such as benzoic acid and KCl) in the MOF crystallization (route c) was also investigated. Pure $Ag_2(BDC)$ monocline crystals were obtained through route a (a-AgMOF) in 10 h, through route b in 5 h, and with the addition of KCl (6 mM) (route c) in 3 h. A mixed system consisting of $Ag_2(BDC)$ monocline crystals and a secondary phase with needle crystals was obtained in 3 h using routes b (b-AgMOF) and c with low additive concentrations. All the synthesized materials possess antibacterial properties against Gram-positive and Gram-negative bacteria.

The b-AgMOF exhibited a MIC of 7.8 μg mL^{-1} and 31.3 μg mL^{-1} for Gram-negative and Gram-positive bacteria, respectively. The two c-AgMOF exhibited instead a MIC of 31.3 μg mL^{-1} and 62.6 μg mL^{-1} for Gram-negative and Gram-positive bacteria, respectively. The observed differences in MIC and MIB values can be attributed to the different morphologies and, in turn, to the different surface areas. Note in addition that the MIC values of the two types of c-AgMOF are comparable with the values reported for other antibacterial materials (Table 1), whilst b-AgMOF shows better antibacterial properties compared to the previous literature data. In addition, a long-term antibacterial effect was observed for b-AgMOF. After 12 weeks, both MIC and MBC lose one dilution factor to 15.6 μg mL^{-1} and 62.5 μg mL^{-1} for Gram-negative and -positive bacteria, respectively. For all the Ag_2BDC MOFs studied, excellent bacteriostatic and bactericidal activities as well as a long-term efficiency were observed, confirming the applicability of Ag_2BDC as a long-term reserve of ions with antibacterial activity. In addition, our data suggest that size plays a marginal role with respect to the long-term efficiency of the AgMOFs both in water and in a culture medium. In fact, despite their size in the range of 1–10 μm much larger than the optimal dimensions of AgNPs (1–10 μm), they act as a reservoir for the release of silver ions, resulting from *in vitro* stability, in terms of antibacterial activity. Finally, with reference to the b-AgMOF, our data would indicate a good compromise between bactericidal activity and the slow-release Ag$^+$ rate, suggesting that the metal organic framework could be considered as a good metal ion reservoir for long-term antibacterial applications, highly stable even under physiological conditions, such as medical ones.

Conflicts of interest

There are no conflicts to declare.

Acknowledgements

The authors thank the Bio-nanotech Research and Innovation Tower (BRIT) laboratory of the University of Catania (grant no. PONa3_00136 financed by the MIUR) for the Smartlab diffractometer and the 5000 Versa Probe X-ray photoelectron Spectrometer. V. P. thanks "Ministero dell'università e della ricerca (MUR)" within the "PON Ricerca e Innovazione 2014-2020 Azioni IV.4" program for support with PhD scolarship DOT1308583 – 2.

References

1 C. J. Murray, K. S. Ikuta, F. Sharara, L. Swetschinski, G. Robles Aguilar, A. Gray, C. Han, C. Bisignano, P. Rao, E. Wool, S. C. Johnson, A. J. Browne, M. G. Chipeta, F. Fell, S. Hackett, G. Haines-Woodhouse, B. H. Kashef Hamadani, E. A. P. Kumaran, B. McManigal, R. Agarwal, S. Akech, S. Albertson, J. Amuasi, J. Andrews, A. Aravkin, E. Ashley, F. Bailey, S. Baker, B. Basnyat, A. Bekker, R. Bender, A. Bethou, J. Bielicki, S. Boonkasidecha, J. Bukosia, C. Carvalheiro, C. Castañeda-Orjuela, V. Chansamouth, S. Chaurasia, S. Chiurchiù, F. Chowdhury, A. J. Cook, B. Cooper, T. R. Cressey, E. Criollo-Mora, M. Cunningham, S. Darboe, N. P. J. Day, M. de Luca, K. Dokova, A. Dramowski, S. J. Dunachie, T. Eckmanns, D. Eibach, A. Emami, N. Feasey, N. Fisher-Pearson, K. Forrest, D. Garrett, P. Gastmeier, A. Z. Giref, R. C. Greer, V. Gupta, S. Haller, A. Haselbeck, S. I. Hay, M. Holm, S. Hopkins, K. C. Iregbu, J. Jacobs, D. Jarovsky, F. Javanmardi, M. Khorana, N. Kissoon, E. Kobeissi, T. Kostyanev, F. Krapp, R. Krumkamp, A. Kumar, H. H. Kyu, C. Lim, D. Limmathurotsakul, M. J. Loftus, M. Lunn, J. Ma, N. Mturi, T. Munera-Huertas, P. Musicha, M. M. Mussi-Pinhata, T. Nakamura, R. Nanavati, S. Nangia, P. Newton, C. Ngoun, A. Novotney, D. Nwakanma, C. W. Obiero, A. Olivas-Martinez, P. Olliaro, E. Ooko, E. Ortiz-Brizuela, A. Y. Peleg, C. Perrone, N. Plakkal, A. Ponce-de-Leon, M. Raad, T. Ramdin, A. Riddell, T. Roberts, J. V. Robotham, A. Roca, K. E. Rudd, N. Russell, J. Schnall, J. A. G. Scott, M. Shivamallappa, J. Sifuentes-Osornio, N. Steenkeste, A. J. Stewardson, T. Stoeva, N. Tasak, A. Thaiprakong, G. Thwaites, C. Turner, P. Turner, H. R. van Doorn, S. Velaphi, A. Vongpradith, H. Vu, T. Walsh, S. Waner, T. Wangrangsimakul, T. Wozniak, P. Zheng, B. Sartorius, A. D. Lopez, A. Stergachis, C. Moore, C. Dolecek and M. Naghavi, *The Lancet*, 2022, **399**, 629–655.

2 M. S. Mulani, E. E. Kamble, S. N. Kumkar, M. S. Tawre and K. R. Pardesi, *Front. Microbiol.*, 2019, **10**, 539.

3 L. B. Rice, *J. Infect. Dis.*, 2008, **197**, 1079–1081.

4 N. Høiby, T. Bjarnsholt, M. Givskov, S. Molin and O. Ciofu, *Int. J. Antimicrob. Agents*, 2010, **35**, 322–332.

5 O. Pacios, L. Blasco, I. Bleriot, L. Fernandez-Garcia, M. González Bardanca, A. Ambroa, M. López, G. Bou and M. Tomás, *Antibiotics*, 2020, **9**, 65.

6 G. Laghi, D. Franco, G. G. Condorelli, R. Gallerani, S. Guglielmino, R. Laurita, D. Morganti, F. Traina, S. Conoci and M. Gherardi, *Plasma Processes Polym.*, 2023, **20**, e2200194.

7 G. Vimbela, S. M. Ngo, C. Fraze, L. Yang and D. A. Stout, *Int. J. Nanomed.*, 2017, **12**, 3941–3965.

8 G. Nocito, E. L. Sciuto, D. Franco, F. Nastasi, L. Pulvirenti, S. Petralia, C. Spinella, G. Calabrese, S. Guglielmino and S. Conoci, *Nanomaterials*, 2022, **12**, 885.

9 S. Agnihotri and N. K. Dhiman, Advances in Biomaterials for Biomedical Applications, in *Advanced Structured Materials*, ed. A. Tripathi and J. Melo, Springer, Singapore, 2017, vol. 66, pp. 479–545.

10 D. Franco, G. Calabrese, S. P. P. Guglielmino and S. Conoci, *Microorganisms*, 2022, **10**, 1778.

11 M. Sakamoto, J. Y. Ha, S. Yoneshima, C. Kataoka, H. Tatsuta and S. Kashiwada, *Arch. Environ. Contam. Toxicol.*, 2015, **68**, 500–509.

12 C. Beer, R. Foldbjerg, Y. Hayashi, D. S. Sutherland and H. Autrup, *Toxicol. Lett.*, 2012, **208**, 286–292.

13 G. Calabrese, G. De Luca, D. Franco, D. Morganti, M. G. Rizzo, A. Bonavita, G. Neri, E. Fazio, F. Neri, B. Fazio, F. Crea, A. A. Leonardi, M. J. Lo Faro, S. Guglielmino and S. Conoci, *Biomater. Adv.*, 2023, **145**, 213193.

14 G. Calabrese, S. Petralia, C. Fabbi, S. Forte, D. Franco, S. Guglielmino, E. Esposito, S. Cuzzocrea, F. Traina and S. Conoci, *Regen Biomater.*, 2020, **7**, 461–469.

15 O. M. Yaghi, M. O'Keeffe, N. W. Ockwig, H. K. Chae, M. Eddaoudi and J. Kim, *Nature*, 2003, 423.

16 A. Hamad, K. S. Khashan and A. Hadi, *J. Inorg. Organomet. Polym. Mater.*, 2020, **30**, 4811–4828.

17 D. Franco, G. Calabrese, S. Petralia, G. Neri, C. Corsaro, L. Forte, S. Squarzoni, S. Guglielmino, F. Traina, E. Fazio and S. Conoci, *Molecules*, 2021, **26**, 1099.

18 X. Y. Li, H. F. Su, K. Yu, Y. Z. Tan, X. P. Wang, Y. Q. Zhao, D. Sun and L. S. Zheng, *Nanoscale*, 2015, **7**, 8284–8288.

19 C. E. Albers, W. Hofstetter, K. A. Siebenrock, R. Landmann and F. M. Klenke, *Nanotoxicology*, 2013, **7**, 30–36.

20 G. Calabrese, S. Petralia, D. Franco, G. Nocito, C. Fabbi, L. Forte, S. Guglielmino, S. Squarzoni, F. Traina and S. Conoci, *Mater. Sci. Eng., C*, 2021, **118**, 111394.

21 H. Liu, S. Battiato, A. L. Pellegrino, P. Paoli, P. Rossi, C. Jiménez, G. Malandrino and D. Muñoz-Rojas, *Dalton Trans.*, 2017, **46**, 10986–10995.
22 B. L. T. Lau, W. C. Hockaday, K. Ikuma, O. Furman and A. W. Decho, *Colloids Surf., A*, 2013, **435**, 22–27.
23 M. E. Davis, *Nature*, 2002, 417.
24 J. Yang and Y. W. Yang, *Small*, 2020, 16.
25 B. Moulton and M. J. Zaworotko, *Chem. Rev.*, 2001, 101.
26 W. Nong, J. Wu, R. A. Ghiladi and Y. Guan, *Coord. Chem. Rev.*, 2021, **442**, 214007.
27 B. P. Xie, J. W. Chai, C. Fan, J. H. Ouyang, W. J. Duan, B. Sun, J. Chen, L. X. Yuan, X. Q. Xu and J. X. Chen, *ACS Appl. Bio Mater.*, 2020, **3**, 8525–8531.
28 M. D. Firouzjaei, A. A. Shamsabadi, M. Sharifian Gh, A. Rahimpour and M. Soroush, *Adv. Mater. Interfaces*, 2018, **5**, 1701365.
29 X. Lu, J. Ye, D. Zhang, R. Xie, R. F. Bogale, Y. Sun, L. Zhao, Q. Zhao and G. Ning, *J. Inorg. Biochem.*, 2014, **138**, 114–121.
30 S. S. Zhang, X. Wang, H. F. Su, L. Feng, Z. Wang, W. Q. Ding, V. A. Blatov, M. Kurmoo, C. H. Tung, D. Sun and L. S. Zheng, *Inorg. Chem.*, 2017, **56**, 11891–11899.
31 D. Sun, R. Cao, W. Bi, J. Weng, M. Hong and Y. Liang, *Inorganica Chim Acta*, 2004, **357**, 991–1001.
32 A. Tăbăcaru, C. Pettinari, F. Marchetti, C. di Nicola, K. V. Domasevitch, S. Galli, N. Masciocchi, S. Scuri, I. Grappasonni and M. Cocchioni, *Inorg. Chem.*, 2012, **51**, 9775–9788.
33 N. A. Travlou, M. Algarra, C. Alcoholado, M. Cifuentes-Rueda, A. M. Labella, J. M. Lázaro-Martínez, E. Rodríguez-Castellón and T. J. Bandosz, *ACS Appl. Bio. Mater.*, 2018, **1**, 693–707.
34 M. Berchel, T. le Gall, C. Denis, S. le Hir, F. Quentel, C. Elléouet, T. Montier, J.-M. Rueff, J.-Y. Salaün, J.-P. Haelters, G. B. Hix, P. Lehn and P.-A. Jaffrès, *New J. Chem.*, 2011, **35**, 1000.
35 S. Arun Kumar, B. Balasubramaniam, S. Bhunia, M. K. Jaiswal, K. Verma, Prateek, A. Khademhosseini, R. K. Gupta and A. K. Gaharwar, *Wiley Interdiscip. Rev.: Nanomed. Nanobiotechnol.*, 2021, **13**, e1674.
36 Y. Sun, L. Zheng, Y. Yang, X. Qian, T. Fu, X. Li, Z. Yang, H. Yan, C. Cui and W. Tan, *Nanomicro Lett*, 2020, 12.
37 G. Chedid and A. Yassin, *Nanomaterials*, 2018, 8.
38 J. Chen, Y. Zhu and S. Kaskel, *Angew. Chem., Int. Ed.*, 2021, 60.
39 M. Ahmadi, S. M. Ayyoubzadeh, F. Ghorbani-Bidkorbeh, S. Shahhosseini, S. Dadashzadeh, E. Asadian, M. Mosayebnia and S. Siavashy, *Heliyon*, 2021, 7.
40 H. Wang, Y. Ma, R. Wang, J. Key, V. Linkov and S. Ji, *Chem. Commun.*, 2015, **51**, 3570–3573.
41 X. Wang, S. Huo, R. Wang, H. Wang, D. J. L. Brett and S. Ji, *J. Colloid Interface Sci.*, 2017, **503**, 76–85.
42 J. A. Kaduk, *Acta Crystallogr B*, 2000, **56**, 474–485.
43 K. Nakamoto, *Infrared and Raman Spectra of Inorganic and Coordination Compounds*, John Wiley & Sons, 1997.
44 C. Tudisco, M. T. Cambria, F. Sinatra, F. Bertani, A. Alba, A. E. Giuffrida, S. Saccone, E. Fantechi, C. Innocenti, C. Sangregorio, E. Dalcanale and G. G. Condorelli, *J. Mater. Chem. B*, 2015, **3**, 4134–4145.
45 C. Tudisco, V. Oliveri, M. Cantarella, G. Vecchio and G. G. Condorelli, *Eur J. Inorg. Chem.*, 2012, **2012**, 5323–5331.
46 D. Briggs and G. Beamson, *Anal. Chem.*, 1992, **64**, 1729–1736.
47 G. G. Condorelli, A. Motta, I. L. Fragalà, F. Giannazzo, V. Raineri, A. Caneschi and D. Gatteschi, *Angew. Chem., Int. Ed.*, 2004, **43**, 4081–4084.
48 G. G. Condorelli, A. Motta, M. Favazza, P. Nativo, I. L. Fragalà and D. Gatteschi, *Chem. – Eur. J.*, 2006, **12**, 3558–3566.
49 D. Briggs and G. Beamson, *Anal. Chem.*, 1993, **65**, 1517–1523.
50 Y. Dong and J. Zheng, *Chem. Eng. J.*, 2020, **392**, 123690.
51 F. Monforte, M. Falsaperna, A. L. Pellegrino, C. Bongiorno, A. Motta, G. Mannino and G. G. Condorelli, *J. Phys. Chem. C*, 2019, **123**, 28836–28845.
52 H. Zhao, L. Yu, L. Zhang, L. Dai, F. Yao, Y. Huang, J. Sun and J. Zhu, *ACS Sustainable Chem. Eng.*, 2021, **9**, 10892–10901.
53 C. R. Marshall, E. E. Timmel, S. A. Staudhammer and C. K. Brozek, *Chem. Sci.*, 2020, **11**, 11539–11547.
54 X. Zhang, X. Shi, Q. Zhao, Y. Li, J. Wang, Y. Yang, F. Bi, J. Xu and N. Liu, *Chem. Eng. J.*, 2022, **427**, 131573.
55 H. Zhang, J. Li, Z. Li, Y. Song, S. Zhu, J. Wang, Y. Sun, X. Zhang and B. Lin, *J. Phys. Chem. Solids*, 2022, **160**, 110336.
56 F. E. Chen, T. A. Pitt, D. J. Okong'o, L. G. Wetherbee, J. J. Fuentes-Rivera and P. J. Milner, *Chem. Mater.*, 2022, **34**, 3383–3394.
57 J. Sun, J. Wan, Y. Wang, Z. Yan, Y. Ma, S. Ding, M. Tang and Y. Xie, *J. Hazard. Mater.*, 2022, **429**, 128299.
58 M. Godoy-Gallardo, U. Eckhard, L. M. Delgado, Y. J. D. de Roo Puente, M. Hoyos-Nogués, F. J. Gil and R. A. Perez, *Bioact Mater*, 2021, **6**, 4470–4490.
59 T. Ishida, *MOJ Toxicol*, 2018, **4**, 345–350.
60 T. C. Dakal, A. Kumar, R. S. Majumdar and V. Yadav, *Front. Microbiol.*, 2016, **7**, 1831.
61 H. Le Pape, F. Solano-Serena, P. Contini, C. Devillers, A. Maftah and P. Leprat, *J. Inorg. Biochem.*, 2004, **98**, 1054–1060.
62 N. Joshi, B. T. Ngwenya, I. B. Butler and C. E. French, *J. Hazard. Mater.*, 2015, **287**, 51–58.
63 Y. Li, X. Xia, W. Hou, H. Lv, J. Liu and X. Li, *Int. J. Nanomed.*, 2023, **18**, 1109–1128.
64 N. Bhardwaj, S. K. Pandey, J. Mehta, S. K. Bhardwaj, K.-H. Kim and A. Deep, *Toxicol Res (Camb)*, 2018, **7**, 931–941.
65 D. Medina Cruz, G. Mi and T. J. Webster, *J. Biomed. Mater. Res. A*, 2018, **106**, 1400–1412.
66 R. Li, T. Chen and X. Pan, *ACS Nano*, 2021, **15**, 3808–3848.
67 A. Abbaszadegan, Y. Ghahramani, A. Gholami, B. Hemmateenejad, S. Dorostkar, M. Nabavizadeh and H. Sharghi, *J. Nanomater.*, 2015, **2015**, 1–8.
68 Y. N. Slavin, J. Asnis, U. O. Häfeli and H. Bach, *J Nanobiotechnology*, 2017, **15**, 65.
69 O. Huisman, R. D'Ari and S. Gottesman, *Proc. Natl. Acad. Sci. U. S. A.*, 1984, **81**, 4490–4494.
70 H. Bao, X. Yu, C. Xu, X. Li, Z. Li, D. Wei and Y. Liu, *PLoS One*, 2015, **10**, e0122535.

71 J. A. Lemire, J. J. Harrison and R. J. Turner, *Nat. Rev. Microbiol.*, 2013, **11**, 371–384.

72 M. Godoy-Gallardo, U. Eckhard, L. M. Delgado, Y. J. D. de Roo Puente, M. Hoyos-Nogués, F. J. Gil and R. A. Perez, *Bioact Mater*, 2021, **6**, 4470–4490.

73 R. E. Duval, J. Gouyau and E. Lamouroux, *Nanomaterials*, 2019, **9**, 1775.

74 R. I. MacCuspie, *J. Nanopart. Res.*, 2011, **13**, 2893–2908.

75 A. Boughbina-Portolés, L. Sanjuan-Navarro, Y. Moliner-Martínez and P. Campíns-Falcó, *Nanomaterials*, 2021, **11**, 926.

76 A. M. el Badawy, T. P. Luxton, R. G. Silva, K. G. Scheckel, M. T. Suidan and T. M. Tolaymat, *Environ. Sci. Technol.*, 2010, **44**, 1260–1266.

77 A. Fiorati, A. Bellingeri, C. Punta, I. Corsi and I. Venditti, *Polymers (Basel)*, 2020, **12**, 1635.

78 L. Wang, C. Hu and L. Shao, *Int. J. Nanomed.*, 2017, **12**, 1227–1249.

79 G. A. Sotiriou, A. Teleki, A. Camenzind, F. Krumeich, A. Meyer, S. Panke and S. E. Pratsinis, *Chem. Eng. J.*, 2011, **170**, 547–554.

80 V. K. Sharma, C. M. Sayes, B. Guo, S. Pillai, J. G. Parsons, C. Wang, B. Yan and X. Ma, *Sci. Total Environ*, 2019, **653**, 1042–1051.

81 C. Levard, S. Mitra, T. Yang, A. D. Jew, A. R. Badireddy, G. V. Lowry and G. E. Brown, *Environ. Sci. Technol.*, 2013, **47**, 5738–5745.

82 Y. Liu, X. Xu, Q. Xia, G. Yuan, Q. He and Y. Cui, *Chem. Commun.*, 2010, **46**, 2608.

83 X. Lu, J. Ye, Y. Sun, R. F. Bogale, L. Zhao, P. Tian and G. Ning, *Dalton Trans.*, 2014, **43**, 10104.